The relationship between bulk-mass momentum and short-period seismic radiation in catastrophic landslides

Clément Hibert, Göran Ekström, Colin Stark

AGU PUBLICATIONS

JGR

Journal of Geophysical Research: Earth Surface

RESEARCH ARTICLE
10.1002/2016JF004027

Key Points:
- We investigate the link between landslide dynamics and short-period seismic radiation
- We found a strong correlation between the bulk momentum and the short-period signal envelope
- We found a scaling law between the amplitude of the short-period signal and the momentum

Correspondence to:
C. Hibert,
hibert@unistra.fr

Citation:
Hibert, C., G. Ekström, and C. P. Stark (2017), The relationship between bulk-mass momentum and short-period seismic radiation in catastrophic landslides, *J. Geophys. Res. Earth Surface*, *122*, 1201–1215, doi:10.1002/2016JF004027.

Received 15 JUL 2016
Accepted 23 APR 2017
Accepted article online 29 APR 2017
Published online 30 MAY 2017

The relationship between bulk-mass momentum and short-period seismic radiation in catastrophic landslides

Clément Hibert[1,2], Göran Ekström[1], and Colin P. Stark[1]

[1]Lamont-Doherty Earth Observatory, Columbia University, Palisades, New York, USA, [2]Now at Institut de Physique du Globe de Strasbourg/EOST, UMR 7516, CNRS, Strasbourg, France

Abstract The relationship between bulk-mass dynamic properties of catastrophic landslides and the generation of short-period seismic waves is investigated, with a particular focus on the momentum of the landslide mass and the envelope of high-frequency seismograms. Twelve very large landslides that occurred in different geological settings worldwide between 1999 and 2014 are selected for study, based on the existence of detailed descriptions of their force histories, determined from long-period seismic waves (frequency lower than 0.1 Hz), as well as the availability of nearby high-quality short-period seismic recordings. A high average correlation (0.94) is found between the modulus of the landslide momentum and the envelope of the high-frequency seismograms, band-passed filtered between 3 and 10 Hz, recorded on nearby stations. The best correlation is seen during the acceleration phase of each landslide. Comparatively poor average correlation (0.57) is found between the modulus of the landslide force and the seismogram envelopes. A possible scaling between the momentum and the amplitude of short-period radiation is investigated. The maximum amplitudes of short-period seismograms for the nine best recorded landslides are corrected for local attenuation and correlated with the maximum momentum of the landslides. The nine data points scatter around a best fitting line that defines a nearly linear relationship between momentum and peak short-period radiation. It is hypothesized that bulk-mass momentum linearly modulates landslide processes that generate short-period seismic waves but that the efficiency of short-period radiation is highly variable between landslides.

1. Introduction

Landslide failures on the scale of mountains are spectacular, dangerous, and spontaneous, making direct observations hard to obtain. Detection of the occurrence of landslides and measurement of their dynamic properties during runout is a research priority, but a logistical and technical challenge. Seismology has begun to help in several important ways. Taking advantage of the densification of global, regional, and local networks of broadband seismic stations, recent advances now allow the seismic detection and location of landslides in near real time. At the global scale, detection of the long-period surface waves generated by the largest landslides permits the location of events in very remote areas that may otherwise have remained undetected [*Ekström and Stark*, 2013]. Thanks to continuous recording, seismology can also help to reconstruct the chronology of landslides caused by strong environmental forcing, such as the Talas typhoon in Japan [*Yamada et al.*, 2012] or the Morakot typhoon in Taiwan [*Lin et al.*, 2010], and more generally to study the spatiotemporal activity of gravitational instabilities at a regional or a local scale and in different geological contexts [e.g., *Deparis et al.*, 2008; *Helmstetter and Garambois*, 2010; *Dammeier et al.*, 2011, 2016; *Hibert et al.*, 2011, 2014a; *Clouard et al.*, 2013; *Chen et al.*, 2013; *Burtin et al.*, 2013; *Tripolitsiotis et al.*, 2015; *Zimmer and Sitar*, 2015].

In addition to detection and location, seismology can be used to determine dynamic properties of landslides. Inversion of long-period surface waves generated by large landslides yields an estimate of the forces imparted on Earth by the bulk accelerating mass [e.g., *Kanamori et al.*, 1984; *Brodsky et al.*, 2003; *Zhao et al.*, 2012; *Ekström and Stark*, 2013; *Allstadt*, 2013; *Coe et al.*, 2016]. From the inverted forces, landslide properties such as its mass, center-of-mass velocity over time, and trajectory can be determined [*Ekström and Stark*, 2013]. Long-period seismic waves generated by catastrophic landslides have also been modeled and used to constrain numerical simulations [e.g., *Favreau et al.*, 2010; *Moretti et al.*, 2012]. These long-period studies have improved our understanding of catastrophic landslides, but the current methods are applicable only to events that

generate strong signals at periods greater than 10 s. Such long-period seismic waves are recorded only for the largest landslides, which account for a very small proportion of the worldwide occurrence of landslides and other gravitational instabilities.

Recently, interest in the information contained in short-period seismic signals (periods shorter than 1 s) generated by gravitational instabilities has grown. Short-period seismic signals are frequently recorded for gravitational instabilities [e.g., *Suriñach et al.*, 2005; *Deparis et al.*, 2008; *Dammeier et al.*, 2011, 2016; *Clouard et al.*, 2013; *Chen et al.*, 2013; *Burtin et al.*, 2013; *Hibert et al.*, 2014a; *Levy et al.*, 2015; *Tripolitsiotis et al.*, 2015; *Zimmer and Sitar*, 2015], even for small events with a volume of the order of a cubic meter [*Hibert et al.*, 2011], when a seismic station is close by. Challenges associated with short-period signals are that they attenuate rapidly away from the source, and their complexity has thus far precluded inversion and modeling.

Short-period signals generated by landslides and other gravitational instabilities have common features, which are usually an emergent onset, no well-defined peak amplitude, a long duration (tens of seconds), and no distinct phases. These features are thought to be physically related to progressive failure [*McSaveney*, 2002], individual block impact along the runout path [*Norris*, 1994; *Vilajosana et al.*, 2008; *Deparis et al.*, 2008], mass bulking from material entrainment [*Suriñach et al.*, 2005], and, more generally, to the granular-flow nature of these phenomena [e.g., *Ratdomopurbo and Poupinet*, 2000; *Calder et al.*, 2002; *Luckett et al.*, 2002; *Dammeier et al.*, 2011; *Hibert et al.*, 2011]. These characteristic signal features are not dependent on the size of the event and are observed for granular flows with volumes on the order of a few cubic meters [e.g., *Deparis et al.*, 2008; *Vilajosana et al.*, 2008; *Hibert et al.*, 2011] to the largest landslides, with volumes exceeding millions of cubic meters [e.g., *Favreau et al.*, 2010; *Allstadt*, 2013; *Hibert et al.*, 2014b, 2015].

Several studies have aimed at finding relationships between features of short-period seismic signals and the most critical properties of an unknown and potentially hazardous event, such as the volume, the mass, and the runout distance. One of the simplest landslide properties to estimate from the short-period seismic signals is the duration of landslide motion, as it is directly correlated to the duration of the seismic signal if recorded at close stations, as shown by several authors [*Norris*, 1994; *McSaveney*, 2002; *Vilajosana et al.*, 2008; *Deparis et al.*, 2008; *Dammeier et al.*, 2011; *Hibert et al.*, 2011]. This landslide duration estimate can, if an average velocity of the moving mass is known, guide an assessment of the runout distance. Alternatively, if the runout distance is known from direct observations, we can estimate the average velocity of the slide.

Another landslide property that is important for rapid hazard assessment is the volume or the mass of the event. Pioneering studies have sought a relationship between the amplitude of short-period seismic signals and the volume of landslides. *Norris* [1994] has shown that a correlation can be found between the maximum amplitude of seismic signals generated by landslides occurring at Mount Saint Helens and their volume, but only for events with nearly the same runout path. *Deparis et al.* [2008] showed that the scaling between peak amplitude and volume does not work well when comparing landslides occurring in different contexts and with possible different dominant mechanisms. However, the statistical analysis of seismic signals from rockfalls occurring in the Swiss Alps performed by *Dammeier et al.* [2011] showed that the volume of the studied landslides could be predicted well using a multivariate linear regression between landslide properties and features of short-period seismic signal band-pass filtered between 1 and 20 Hz, including its peak amplitude, integrated envelope, and duration. Another approach proposed by *Hibert et al.* [2011] and based on a numerical model and a catalog of 1700 seismic signals of rockfalls recorded at Piton de la Fournaise volcano at distances ranging from hundreds of meters to a few kilometers has shown that the energy of the seismic signals filtered between 1 and 20 Hz is linearly proportional to the potential energy for each event. This proportionality between the seismic and potential energies made it possible to estimate the volume of each rockfall directly from the computed seismic energy.

Recent studies have suggested that the short-period seismic waves generated by landslides also carry information on their dynamics. *Schneider et al.* [2010] compared numerical models of the Iliamna and the Aroaki/Mount Cook rock-ice avalanches to the associated short-period seismic signals and showed that a good correlation exists between the short-period seismic signal envelope and the modeled friction work rate at the base of the avalanches. Using another model-based approach, *Levy et al.* [2015] showed that a correlation can be found between the modeled basal force applied on the ground and the power of the short-period seismic signal (which is the seismic energy computed as the integral of the squared amplitude of the envelope on a moving window) for rockfalls that occurred at Soufrière Hills volcano on Montserrat Island.

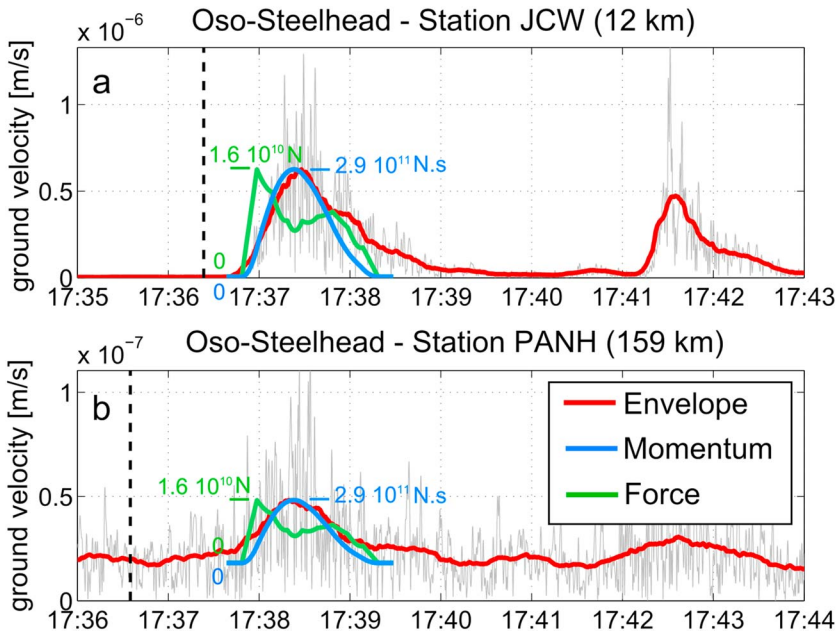

Figure 1. Raw (grey) and smoothed (red) envelope of the short-period signal band-pass filtered between 3 and 10 Hz generated by the Oso landslide and recorded on (a) JCW station and (b) PANH station, along with the modulus of the landslide momentum (blue) and of the modulus of the force of the landslide imparted to the ground (green), and their maximum values, inferred from inversion of long-period seismic surface waves.

All of these case studies give insights into potential linkages between short-period seismic signals and the dynamics of gravitational instabilities, but we still lack an understanding of what the dominant physical processes are that control the amplitude of the short-period-wave radiation generated by slope failures in general. Key questions persist, such as the following: Are the features of short-period seismic signal determined by the bulk dynamics or are they dominated by the sum of stochastic phenomena, such as individual particles interacting with the topography? If there is a link between the large-scale dynamics of a landslide and the genesis of short-period waves, what could be the dynamic parameters that control the amplitude of the seismic signals? And finally, if such a correlation exists, is it generalizable to landslides that occur in different contexts and with different rheologies?

In a recent study of the catastrophic 2014 Oso, Washington, landslide [*Hibert et al.*, 2015], we made a new observation relevant to these questions. We found that the normalized envelope of the short-period seismic signal is very similar to the temporal evolution of the modulus of the normalized momentum of the center of mass inferred from inversion of the long-period seismic waves. This similarity is observed at the closest stations (Figure 1a) and also at stations located dozens of kilometers from the source (Figure 1b). Poor correlation is observed between the modulus of the inverted force exerted by the landslide on the solid Earth and the envelope of the short-period seismic signal (Figure 1). This observation leads to the specific questions addressed in this paper: Is the similarity between center-of-mass momentum and the short-period signal amplitude observed for the Oso landslide unusual, or characteristic of catastrophic landslides? And, more generally, what is the relationship between the center-of-mass dynamics, deduced from long-period inversions, and first-order features of the short-period seismic signals?

2. Data and Analysis

To investigate the relationship between the bulk dynamics of large landslides and their associated short-period seismic radiation, we first identified landslides for which landslide force histories (LFHs) have been determined, and for which high-quality short-period seismograms are available. Since short-period radiation from landslides is relatively weak, the latter condition translates into a selection of events for which a seismic station is located within ~150 km distance. We found seven landslides that meet these criteria in the compilation of *Ekström and Stark* [2013] (the Akatani, Fangtunshan, Mount Steller, Mount Steele, Mount Lituya, Hsiaolin, and Sheemahant Glacier landslides) and three additional ones in our two recent studies

[*Hibert et al.*, 2014b, 2015] (the Oso-Steelhead and the two Bingham Canyon Mine landslides). In addition to these 10, we determined new LFHs for two landslides that have not previously been investigated (the Mount Dall and Hubbard landslides). Estimation of the force history of a landslide is possible when it generates long-period surface waves (< 40 s) with sufficient amplitudes to be recorded on several stations. This criterion is controlled mainly by the size of the event and by the level of the background noise at the time of the landslide. The smallest event for which we have been able to determine a LFH is the main Oso-Steelhead event, with a volume of $\sim 7-10 \times 10^6$ m^3 [*Keaton et al.*, 2014; *Hibert et al.*, 2015].

The total number of landslides is therefore 12. Six of the 12 landslides occurred in glacial environment and on glaciers (the Mount Steller, Mount Steele, Mount Lituya, Mount Dall, Hubbard, and Sheemahant Glacier landslides), four are linked to strong bouts of rain in temperate or tropical environments (the Akatani, Fangtunshan, Hsiaolin, and Oso-Steelhead landslides), and two are related to human activity (the two Bingham Canyon Mine landslides). For all of these, short-period seismograms are available at distances smaller than 152 km; for six of the landslides the nearest station is closer than 30 km. Details of the individual landslides can be found in Appendix A.

For each landslide, we use the LFH results to infer bulk dynamic properties of the landslide, such as momentum and speed, following the approach developed by *Ekström and Stark* [2013]. We use envelopes of short-period band-pass-filtered vertical-component seismograms to characterize the short-period radiation.

2.1. Long-Period Analysis

The long-period analysis of the 12 landslides investigated here follows the methodology developed and applied in our earlier papers [*Ekström and Stark*, 2013; *Hibert et al.*, 2014b], and we refer the reader to these earlier studies for a technical description of the approach. Here we briefly summarize the phenomenology and the physics that allow us to determine the landslide momentum from observed seismic waves. The acceleration and deceleration of the bulk mass during a landslide cause an unloading and loading of the slope that generates long-period seismic waves. The forces acting on the slide mass that bring about this unloading-loading cycle are gravity, basal friction, and centripetal forces, and each of these has a reactive counterpart acting on the solid Earth in the opposite direction across the slide contact area. The landslide therefore exerts a force **F** on the solid Earth that is the vector opposite of the force $\mathbf{F}_S$, equivalent to the bulk momentum change of the slide:

$$\mathbf{F}[\mathbf{x}, t] = -\mathbf{F}_S = -\frac{\mathrm{d}(m\mathbf{v})}{\mathrm{d}t}[\mathbf{x}, t] \ . \tag{1}$$

The time-varying forces acting on the slope during the unloading-loading cycle can be retrieved by inversion of long-period seismic waves and thereby provide a force history from which information on the dynamics of the landslide can be inferred. We use the inversion method developed by *Ekström and Stark* [2013]. The method is based on the approximation that when considering the long-period signals, the landslide seismic source can be described as a time-varying, 3-D force vector acting at a fixed point [*Kanamori and Given*, 1982; *Fukao*, 1995; *Brodsky et al.*, 2003; *Ekström and Stark*, 2013; *Allstadt*, 2013]. This assumption is justified to the extent that the spatial scale of the slide is small compared to the wavelength of the seismic waves and to the distances to the recording seismic stations. Hence, we generally restrict our analysis to signals with periods longer than 40 s, which have wavelengths exceeding 100 km, while large landslides have runout distances of a few kilometers. The three-component force histories for the 12 landslides investigated here are shown in Figure A1, and Table A1 provides key descriptive parameters for each slide, such as the total duration, maximum force, and maximum momentum.

To obtain the time-varying momentum $\mathbf{p}[t]$ of the landslide, the force history $\mathbf{F}[t]$ is integrated over time,

$$\mathbf{p}[t] = -\int_0^t \mathbf{F}[\tau]\,\mathrm{d}\tau \ . \tag{2}$$

Note that no additional information about the landslide, beyond the LFH, is needed to derive the center-of-mass momentum time history.

2.2. Short-Period Analysis

We collect short-period seismograms from stations close to the landslide in order reduce the influence of wave propagation on our observations. We remove the instrument response to restore ground velocity. Since some of the landslides were recorded only on vertical-component seismometers at short distances, we restrict

Table 1. Correlation Coefficients Between Short-Period Seismic Signal Envelope, Inverted Center-of-Mass Momentum, and Inverted Force Modulus and Optimal Apparent Wave-Propagation Velocity Used to Align the Short-Period Seismogram With the Momentum Time History.

Name	Network Station (Distance to Source Kilometer)	Correlation Coefficient $\|p\|$ (3–10 Hz)	Correlation Coefficient $\|p\|$ (1–3 Hz)	Correlation Coefficient $\|F\|$ (3–10 Hz)	Correlation Coefficient $\|F\|$ (1–3 Hz)	V_s (10^3 m s^{-1})
Akatani	Hi-NET HZNH (17)	0.94	0.83	0.67	0.39	0.9
Bingham #1	UU NOQ (13)	0.96	0.70	0.76	0.61	3.0
Bingham #2	UU NOQ (13)	0.91	0.47	0.60	0.17	3.0
Fāngtúnshān	TW MASB (19)	0.95	0.87	0.65	0.66	1.1
Hsiǎolín	TW YULB (70)	0.95	0.85	0.33	0.42	1.1
Hubbard	AK SAMH (71)	0.95	0.95	0.44	0.38	1.8
Mount Dall	YU BYR (115)	0.87	0.46	0.76	0.34	3.4
Mount Lituya	AT SKAG (140)	0.91	0.94	0.55	0.52	3.7
Mount Steele	AK LOGN (49)	0.93	0.95	0.48	0.52	2.6
Mount Steller	AK GRIN (26)	0.98	0.95	0.70	0.57	0.9
Oso-Steelhead	UW JCW (12)	0.98	0.78	0.61	0.47	1.1
Sheemahant Glacier	CN BBB (152)	0.98	0.96	0.34	0.24	2.8
Average	-	0.94	0.81	0.57	0.44	-

our analysis to the vertical component. Also, the frequency range shared by recordings of the landslides was constrained by a sampling rate of 20 Hz at some of the stations. We therefore band-pass filter all of the signals between 1 Hz and 10 Hz using a Butterworth filter with eight poles and eight zeros. The envelopes of the signals are computed using a Hilbert transform.

We compare the envelope of the short-period signal to the absolute value of the landslide momentum, as inferred from the LFH inversion. To make the comparison, we need to apply a correction for the propagation time of the short-period signal from the landslide to the recording station. For short-period surface waves in the 1–10 Hz frequency band, propagation velocities are highly variable and dependent on shallow geology as well as topography. However, the closer the station is to the source, the smaller the impact of uncertainties in the propagation velocity will be on the alignment of the two signals. For example, for a seismic wave propagating at 1000 m s^{-1} but assumed to travel at 1500 m s^{-1}, the traveltime error is only 3.33 s for a station 10 km from the source, but 33.3 s at 100 km from the source. With most landslide signals discussed here having duration greater than a minute, 3.33 s is a relatively small error. In our analysis we therefore selected for analysis and comparison the short-period signal with the best signal-to-noise ratio recorded on the closest stations.

When possible, we computed the apparent wave-propagation velocity by differencing the onset times of the short-period signals filtered between 1 and 10 Hz at two stations aligned with the source, and dividing by the interstation distance. We were able to find aligned stations with the source for four of the landslides (Oso-Steelhead, Mount Steller, and the two Bingham Canyon Mine landslides). For the remaining landslides, we picked a short-period onset time and associated it with the start of the LFH. We confirmed that the second approach resulted in compatible estimates when applied to the four landslides with interstation estimates. The apparent wave-propagation velocities used for alignment of the signals for the 12 landslides are listed in Table 1. We do not make any corrections for propagation dispersion, as the dominant factor controlling the duration of the short-period signal is the duration of sliding, something observed previously [e.g., *Suriñach et al.*, 2005; *Vilajosana et al.*, 2008; *Schneider et al.*, 2010; *Dammeier et al.*, 2011; *Hibert et al.*, 2011] and corroborated by the current study.

2.3. Correlation of Short-Period Seismic Signal Amplitudes and Landslide Momentum

After shifting the short-period signal to account for the time of propagation, we compare the signal envelope and the landslide momentum. Figure 2 shows the two signals plotted on top of each other after normalization of each signal. Since numerous studies have shown that the energy of short-period seismic signals is high above 3 Hz [e.g., *Suriñach et al.*, 2005; *Dammeier et al.*, 2011; *Hibert et al.*, 2011, 2014a; *Levy et al.*, 2015], we initially filter the signals between 3 and 10 Hz and also calculate a smooth envelope using a running-average filter with a length of 1000 samples.

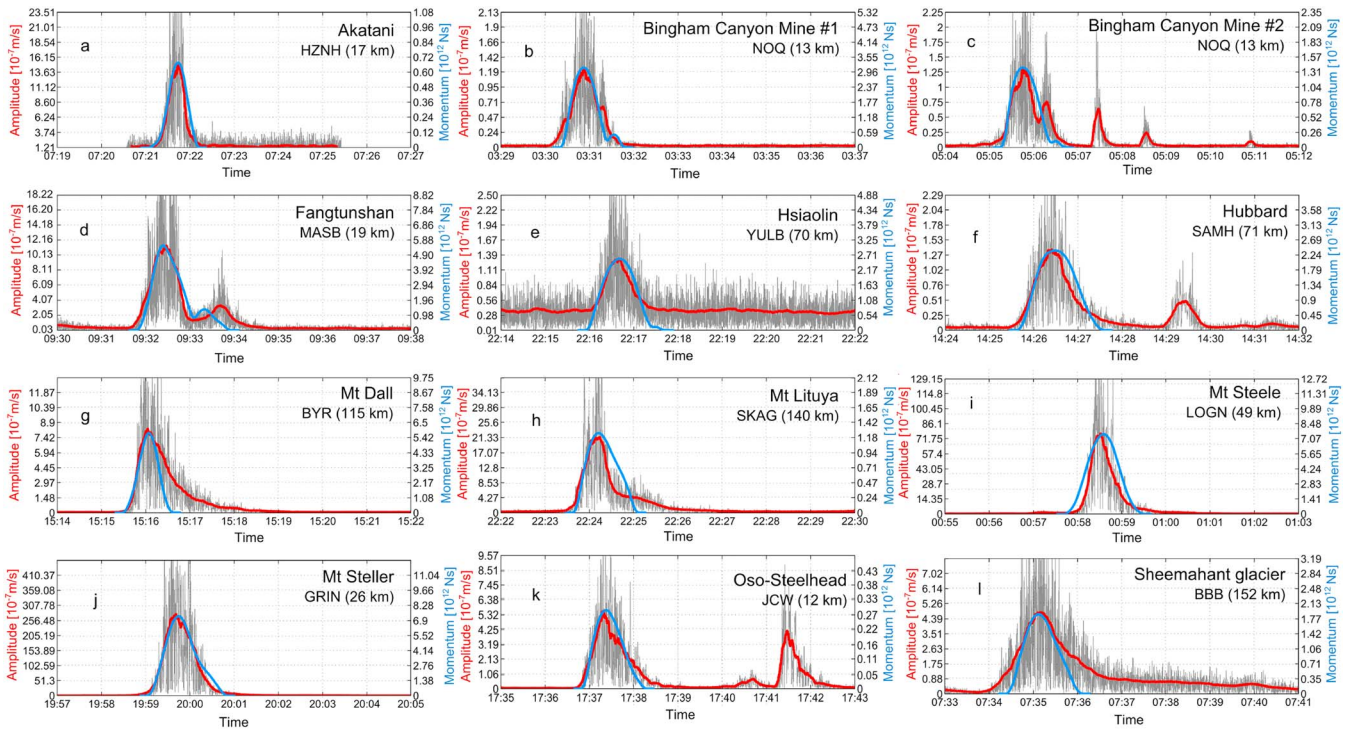

Figure 2. Envelope of the short-period signal filtered between 3 and 10 Hz, smoothed envelope (red) and inverted momentum (blue) for the (a) Akatani, (b) first Bingham Canyon Mine, (c) second Bingham Canyon Mine, (d) Fāngtúnshān, (e) Hsiǎolín, (f) Hubbard, (g) Mount Dall, (h) Mount Lituya, (i) Mount Steele, (j) Mount Steller, (k) Oso-Steelhead, and (l) Sheemahant landslides.

The similarities of the landslide momentum time histories and the smoothed envelopes are visually evident. In particular, the total duration of significant amplitude and the gradual growth from the emergent start to the peak amplitude are very similar for most of the events (Figure 2). The correlation coefficients between the curves range between 0.87 and 0.98 for the 12 landslides, with an average of 0.94 (Table 1), quantifying their qualitative similarity.

To examine the correlation of the two curves in greater detail, we plot the normalized and smoothed short-period signal amplitude as a function of the normalized momentum (Figure 3). For most of the landslides the best correlation of the envelope and the momentum is during the acceleration phase, as can be inferred by the proximity of the points reflecting the early part of the slide to the one-to-one line in Figure 3. Once the peak momentum is reached and deceleration starts, different types of decorrelation behavior are reflected by the deviations from the one-to-one line.

For the first and second Bingham and the Fangtunshan landslides a secondary high-amplitude short-period arrival causes the decorrelation observed during the deceleration phase. For the Mount Dall and Sheemahant Glacier landslides, the momentum returns to zero before the short-period envelope reaches the background noise level. For the Mount Lituya landslide and, to a lesser extent, the Hubbard, Akatani, and Hsiaolin landslides, the short-period envelope decreases faster than the momentum after reaching its maximum.

The correlation between the short-period signal amplitude and the momentum is dependent on the frequencies included. We investigated the short-period envelopes and the correlations using a lower-frequency band-pass filter between 1 and 3 Hz and obtained substantially lower correlations. The average correlation for the 12 landslides is 0.81 (see Table 1). The weaker correlation may be related to stronger attenuation of scattered waves in the 3–10 Hz frequency band than in the 1–3 Hz frequency band, and especially of the coda of those signals [*Aki and Chouet*, 1975].

The focus of the analysis described here is on the momentum, but we also calculated the correlations between the modulus of the force history itself and the smoothed envelopes of the short-period signals. As the force history typically is characterized by an early strong force associated with acceleration, and a late force associated with deceleration, correlations with the bell-shaped short-period signal amplitude envelope are not

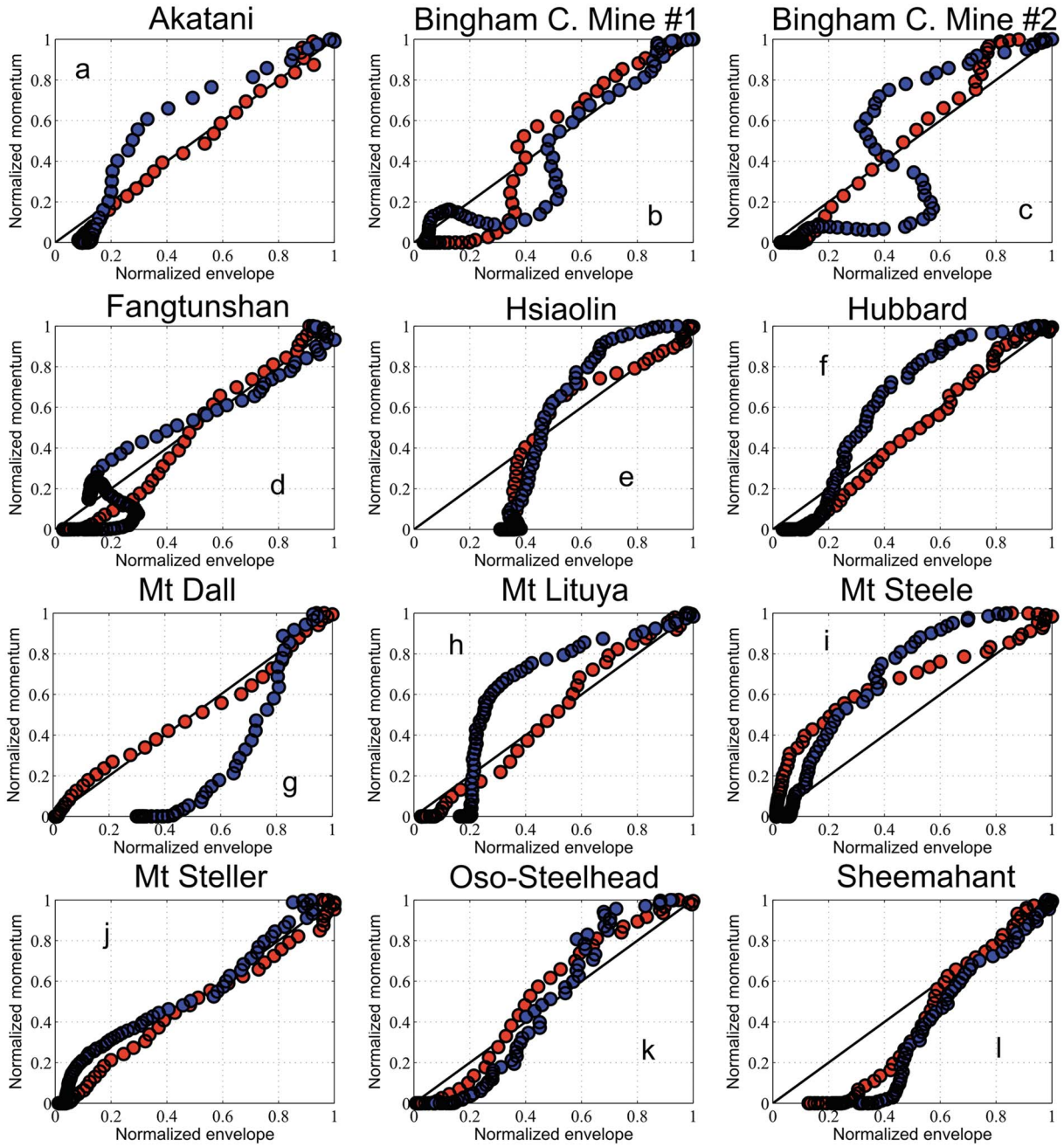

Figure 3. Normalized momentum as a function of the normalized smoothed envelope amplitude for the (a) Akatani, (b) first Bingham Canyon Mine, (c) second Bingham Canyon Mine, (d) Fāngtúnshān, (e) Hsiǎolín, (f) Hubbard, (g) Mount Dall, (h) Mount Lituya, (i) Mount Steele, (j) Mount Steller, (k) Oso-Steelhead, and (l)Sheemahant landslides. The orange circles correspond to the increasing phase of the momentum toward its maximum (acceleration) and the blue circles to the decreasing phase from the maximum to zero (deceleration).

high. The average correlation between the envelope of the seismic signal filtered in the 3–10 Hz band and the modulus of the force is 0.57. This value is significantly lower than the one obtained for the correlation between the envelope and the momentum.

2.4. Quantitative Analysis: An Amplitude-Momentum Scaling Law?

For most of the 12 landslides in our study, a very good correlation exists between the shape of the envelope of the short-period signal and the time history of the landslide momentum. We now investigate the extent to which the amplitude of the short-period signal correlates with the absolute momentum of the landslide.

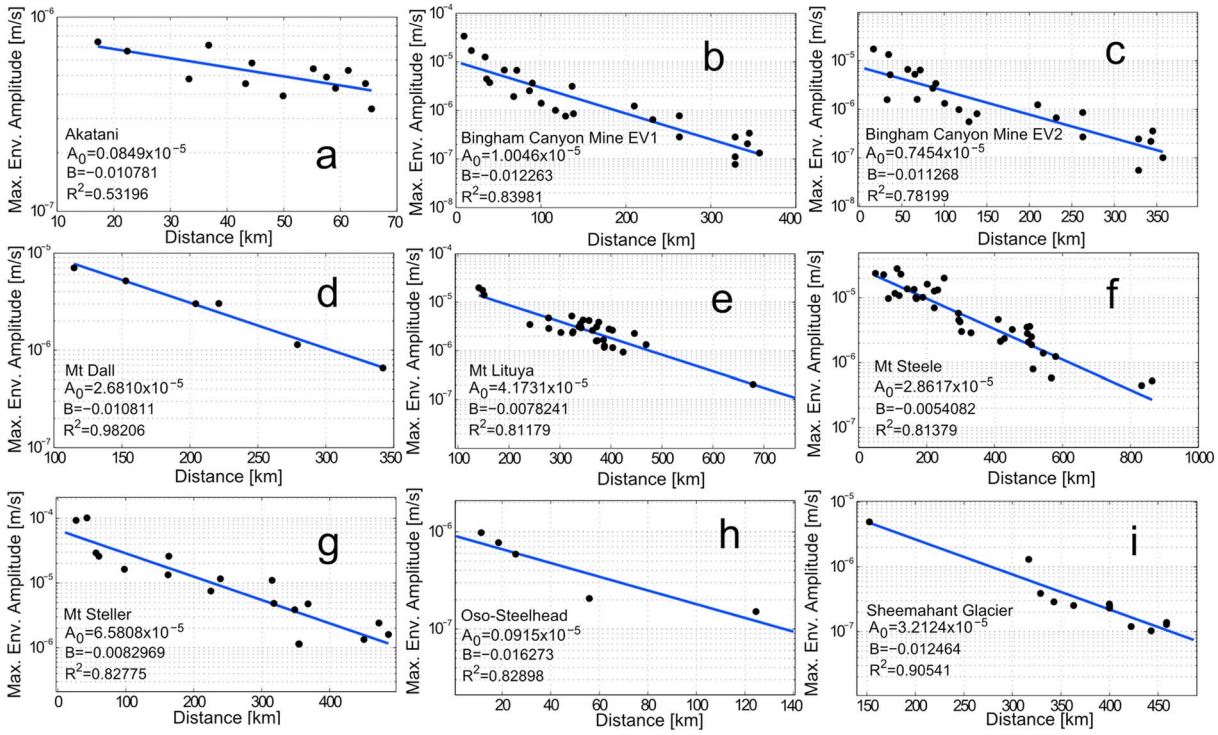

Figure 4. Maximum envelope amplitude recorded at each station as a function of the distance and corresponding fitting curve (blue) for the (a) Akatani, (b) first Bingham Canyon Mine, (c) second Bingham Canyon Mine, (d) Mount Dall, (e) Mount Lituya, (f) Mount Steele, (g) Mount Steller, (h) Oso-Steelhead, and (i) Sheemahant glacier landslides.

Previous studies have suggested different approaches to this problem. For example, *Deparis et al.* [2008] studied 10 rockfalls that occurred between 1992 and 2001 in the French Alps and developed a seismic-magnitude scale for those rockfalls based on the local magnitude defined by *Richter* [1935, 1958] and the 67 seismic records available for the rockfalls. Their proposed magnitude scale is based on a simple attenuation model and the observed peak ground displacement recorded at several stations for a given event. They determined the attenuation model parameters from all of the observations. *Dammeier et al.* [2011] used a similar approach in their study of rockslides but, because of the large number of seismic observations available for their set of events, with most stations at distances less than 100 km, were able to compute individual attenuation parameters for each studied event.

Since most of the 12 landslides in our study have well-recorded short-period signals at several stations, we here follow the approach of *Dammeier et al.* [2011] and estimate landslide-specific propagation corrections. Following *Aki and Richards* [1980], we consider the decrease with distance of the amplitude of a seismic surface wave to be given by the following equation:

$$A(r) = A_0 \frac{e^{-Br}}{\sqrt{r}}, \tag{3}$$

with

$$B = \frac{\pi f}{QV_s}. \tag{4}$$

In equation (3) A_0 is the amplitude of the source, the damping factor B expresses the attenuation due to the anelasticity of the medium, and $1/\sqrt{r}$ expresses the attenuation related to geometrical spreading for surface waves. The parameter B given by equation (4) is a function of the frequency f and the velocity V_s of the seismic waves, and of the quality factor for attenuation Q. Determining the parameters used to compute the factor B is difficult, especially for the frequency range of the seismic waves we study as no global velocity and attenuation models exists for the shallow layers in which these short-period seismic waves propagate. Nevertheless, as we know the distances between the source and the recording stations, we can find, for a given event, the

Table 2. Estimated Attenuation Parameters

Name	A_0 (10^{-5} m s^{-1})	B ($\times 10^{-3}$)	(R^2)
Akatani	0.0849	−10.791	0.53
Bingham #1	1.0046	−12.263	0.84
Bingham #2	0.7454	−11.268	0.78
Mount Dall	2.6810	−10.811	0.98
Mount Lituya	4.1731	−7.8241	0.81
Mount Steele	2.8617	−5.4082	0.81
Mount Steller	6.5808	−8.2669	0.83
Oso-Steelhead	0.0915	−16.273	0.83
Sheemahant Glacier	3.2124	−12.464	0.91

parameters A_0 and B of a curve defined by equation (3) that best fits the distribution of the amplitude as a function of the recording distance from the source. This processing yields, for each event, the source amplitude A_0 and the factor B. We consider B to be constant in the narrow frequency band used in the analysis.

In our analysis we used the maximum amplitude of the smoothed envelope of the short-period signal. For each seismogram, we correct the maximum envelope amplitude $A(r)$ by the geometrical spreading term $1/\sqrt{r}$ and then find the line that best fits the corrected amplitudes in a log-log space with a least squares fitting algorithm (Figure 4). The values of the source amplitude A_0, the factor B, and the R^2 values for each landslide are given in Table 2. For all but the Akatani landslide, the R^2 values are close to 0.8 or above, which shows that our simple attenuation model is capable of fitting the data well. For the Akatani landslide, all the stations that recorded good short-period seismic signal are less than 100 km from the source, and the high variability of the maximum-amplitude values recorded at different stations at similar distance is what causes the R^2 value to be low (0.53).

A limitation of this approach is that we need a sufficient number of stations to obtain a robust fit between the regression curve and the data. For the Hsiǎolín and the Fāngtúnshān landslides, we did not find records of short-period seismic signals on more than three stations, which led us to exclude these events from our quantitative analysis.

For each landslide for which we were able to compute the amplitude corrected from attenuation, we plotted the logarithm of the maximum amplitude A_0 of the seismic signal envelope as a function of the logarithm of the maximum momentum $|p|$ (Figure 5). For the seismic signals showing a high-amplitude late arrival, we consider the first maximum of the envelope and not the second maximum associated with these late arrivals. Most of the points align well with a line, suggesting that the amplitude of the short-period seismic signal scales as a function of the momentum of the center-of-mass as

$$\log(A_0) = \alpha \log(|p|) + \beta, \tag{5}$$

with $\alpha = 1.11 \pm 0.61$ (within a 95% confidence interval), $\beta = -18.42 \pm 7.55$, and $R^2 = 0.72$. However, the points associated with the Mount Lituya and the Sheemahant Glacier landslides are more distant from this

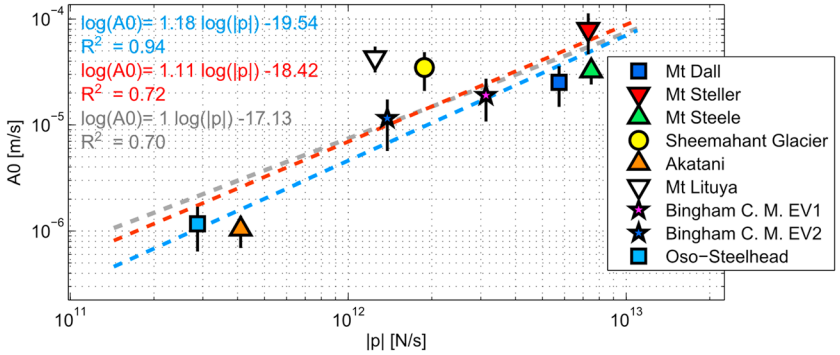

Figure 5. Maximum amplitude A_0 of the short-period seismic signal envelope corrected for attenuation effects as a function of the maximum of the momentum p for nine landslides. The range of values within the 95% confidence interval on the computation of the amplitude A_0 is represented for each landslide by a black line. The dashed red line is the best fit of all the points, the blue dashed line is the best fit while excluding the Mount Lituya and the Sheemahant Glacier landslides, and the grey dashed line is the best fit with $\alpha = 1$.

regression line. When computing a regression line excluding these three landslides, we obtain a coefficient $\alpha = 1.18 \pm 0.34$ and $\beta = -19.54 \pm 4.21$, with $R^2 = 0.94$.

3. Discussion and Conclusion

The results from our analysis of 12 landslides largely agree with the initial observation of good correlation between the time history of short-period signal amplitude and the bulk landslide momentum [*Hibert et al.*, 2015]. While the emergent start of short-period signals of landslides is well known [e.g., *Suriñach et al.*, 2005; *Deparis et al.*, 2008; *Hibert et al.*, 2011; *Dammeier et al.*, 2011], as is their characteristic spindle- or cigar-shaped envelopes, the relationship to bulk properties of the landslide has previously been difficult to investigate due to the lack of time histories of landslide force, speed, or momentum. Access to the landslide force histories obtained through inversion of long-period seismic signals is the development that makes possible the quantitative comparisons detailed above.

On one level, the observed good correlation could be anticipated. Peak momentum can only occur after a period of initial acceleration and before deceleration, making a quasi-symmetric momentum time history, similar to a typical short-period envelope, a natural possibility. However, the consistency of the high-correlation values between the seismic signal envelope and the momentum suggests that there is indeed a causal link behind this correlation. Moreover, when combined with the recent additional observations that the peak force in catastrophic landslides typically occurs early in the landslide [*Allstadt*, 2013; *Hibert et al.*, 2014b], additional inferences can be made. An early peak force strongly argues for rapid mobilization of the full landslide mass. The emergent short-period signal amplitudes are then not consistent with a gradual increase of the sliding mass over time but can logically be associated with the increase in the sliding speed.

In the analysis above, we have focused on the momentum as the bulk property with which to correlate the short-period signal amplitude. Other quantities related to the momentum, such as the center-of-mass kinetic energy, or the squared momentum, have similar bell-shaped time histories and therefore also exhibit good correlation with the short-period envelopes. For example, the average correlation between the squared momentum and the short-period signal envelope is 0.86 (0.94 with the momentum). While we do not believe that the quality of our observations warrant a search for a best fitting dynamic variable, we note that after experimentation with some alternative variables, we were unable to improve on the good average correlation provided by the momentum time histories. It is important to note that the scaling relationship found between the short-period seismic signal and the bulk momentum is dependent on the frequency band. We obtained better correlation in the 3–10 Hz band than in the 1–3 Hz band and were unable, because of limitations of the data, to investigate the correlations at higher frequencies. The relationships between the seismic signal at different frequencies and characteristics of the landslide source are complex and deserve further study.

Our results provide some insight to the key questions posed in section 1 regarding short-period signals generated by gravitational instabilities. In particular, they show that the amplitude of the seismic signal is related to the bulk dynamics (namely momentum) of large landslides and that this is true for landslides occurring in different contexts. However, the physical processes that explain this link are yet to be fully understood.

A linear relationship between landslide bulk momentum and short-period signal amplitude can potentially be seen as reflecting the scaling of small-scale processes within the landslide mass, and between the landslide mass and its substrate. For example, the impulse imparted to the solid Earth by a bouncing rock will be proportional to the momentum of the rock, and the amplitude of the seismic wave will be proportional to the magnitude of the impulse. The rate of particle impacts, which may increase with the speed of the mass, might also have a control on the seismic wave generation. Our results suggest that these hypothetical processes that lead to seismic wave generation have their intensity linearly modulated by the bulk momentum of the landslide. These ideas have to be further investigated by conducting analysis and modeling of the granular processes occurring within landslides, with a particular focus on the link between the bulk dynamics and the magnitude of the impulse of the grains on the slope.

The decorrelation between the momentum and the short-period signal envelope during the deceleration phase can have different explanations, depending on the context in which the landslides occurred. For the Bingham Canyon Mine landslides, a secondary impulse arrival is thought to be caused by the collision of the flowing mass with the pit walls [*Hibert et al.*, 2014b]. For other landslides, such as the Sheemahant Glacier, the Mount Lituya, and the Mount Dall landslides, a failure of the LFH inversion to capture a very gradual

deceleration of the slide, suggested by the very long coda of the short-period seismic signals, may explain the loss of correlation. These three landslides traveled paths that crossed glaciers, which might suggest that a long coda reflects the influence of this kind of substrate on landslide dynamics. Furthermore this long coda is not observed for landslides that do not occurred in glacial environments, such as the Oso, the Akatani, or the Hsiaolin landslides. However, the Mount Steele and Mount Steller landslides also occurred on glaciers and no long coda is observed on the associated seismic signals. These different characteristics may reflect source properties but could potentially also be related to the different distances at which the landslides were recorded (closest recording station at 26 km and 49 km for the Mount Steller and Mount Steele landslides, 115 km, 140 km, and 152 km for the Mount Dall, Mount Lituya, and Sheemahant Glacier landslides, respectively). This demonstrates how difficult it can be to interpret seismic signal features and to relate them to the particular influence of a single factor. Each landslide is unique, and its dynamics are influenced by intricate and complex interactions with the topography and the underlying substrate that require detailed analysis to be understood. Nevertheless, this highlights the fact that short-period seismic waves generated by landslides carry complementary information that cannot be found by solely investigating the long-period seismic radiation.

Our investigation into the existence of a single scaling relationship, applicable to landslides in different settings, produced results that motivate further study. We find support for an approximately linear scaling relationship between momentum and short-period signal amplitude (Figure 5) based on our sample of nine landslides. However, while it is evident that our estimates of source amplitude have significant uncertainty, it seems appropriate to interpret most of the scatter in Figure 5 as reflecting landslide variability.

This line of reasoning would then lead to the suggestion that while, for a given landslide, the amplitude of short-period seismic radiation is proportional to the bulk momentum, landslides have different efficiencies for generating short-period radiation. We hypothesize that factors that control the efficiency include rock type, terrain roughness, substrate rheology and deformability, slope angle, and level of fragmentation, but obviously, there are many other characteristics that can have an influence. New results also suggest that the efficiency might change between the acceleration and the deceleration phase, owing to the orientation of the main direction of motion relative to the normal of the slope (personal communication with Maxime Farin). This might also be one of the factors explaining the decorrelations observed during the deceleration phase, but has to be further investigated.

Our analysis also suggests that for landslides occurring in the same area, following roughly the same runout path and having similar kinematic parameters (acceleration and velocity), a linear scaling between the properties (volume and mass) of the landslides and the features of the seismic signal could be found. This would be a consequence of the momentum-amplitude scaling relationship and could explain the correlations found by *Norris* [1994] between the amplitude and the volume for landslides occurring on the same slope, or by *Hibert et al.* [2011] between the seismic energy and the volume for granular flows occurring on the slopes of the Piton de la Fournaise volcano main crater, which are most of the time of the same length.

The implications of our observations are twofold. First, taking into account the scaling between the amplitude of short-period waves and the momentum of the landslide can help to constrain and to refine the inversion and the modeling of landslide dynamics based on their seismic signals. For example, the envelope of the high-frequency seismic signals can be used in the inversion processes to constrain the duration and the modulus of the inferred momentum. This will also aid the reconstruction of small-scale or low-acceleration motions, which are usually not recovered in the inversion of long-period waves. The envelope of the high-frequency seismic signal could also help calibrate modeling by, for example, comparison of the bulk momentum of the modeled landslide and observed signal envelopes. Second, if this relationship is verified in other contexts and for smaller events, it can help provide estimates of dynamic properties (velocity and runout distance) of smaller gravitational instabilities. As smaller events constitute the large majority of slope failures that occur worldwide, being able to quantify the dynamics for a broader range of the sizes of gravitational instabilities would constitute a breakthrough.

Appendix A: Landslide Catalog

The landslides investigated in this study were selected from the compilation of events published by *Ekström and Stark* [2013], to which we added analyses of the largest events in 2013 and 2014. We omitted nearly two thirds of the potential events due to the lack of nearby short-period seismic recordings. Most of the events

Table A1. Parameters Used for the Inversion, Inverted Maximum Force, and Inferred Dynamic Properties[a]

		Inversion Results				
Name	Source Duration (s)	F_{max} (10^{12} N)	p_{max} (10^{11} kg m s^{-1})	M (10^{9} kg)	a_{max} (m s^{-2})	v_{max} (m s^{-1})
Akatani	70	0.038	0.64	24	1.58	16.88
Bingham #1	90	0.189	3.13	70	2.7	44.74
Bingham #2	90	0.099	1.38	35	2.83	39.50
Fāngtúnshān	105	0.277	5.51	13	2.13	41.15
Hsiǎolín	105	0.096	2.57	6	1.60	42.81
Hubbard	120	0.083	2.37	29	2.86	82.68
Mount Dall	70	0.329	5.74	125	2.63	45.90
Mount Lituya	90	0.067	1.25	29	2.31	45.17
Mount Steele	110	0.272	7.31	108	2.51	69.29
Mount Steller	110	0.277	7.48	135	2.05	54.11
Oso-Steelhead	90	0.016	0.29	15	1.07	19.14
Sheemahant Glacier	105	0.076	1.88	81	0.93	23.20

[a]Note that to calculate M, a_{max}, and v_{max}, independent information on the total runout of the slide is required, while F_{max} and p_{max} result directly from the LFH inversion.

for which we were able to gather a sufficient number of short-period seismograms occurred in dense local or regional networks. A brief description of each landslide is provided below. Table A1 provides key parameters obtained in the long-period analysis, and Figure A1 shows the three-component LFHs for all 12 landslides.

Akatani. The Akatani landslide occurred on 4 September 2011 at 7:21:30 UT and is one of the largest slope failures in a sequence caused by the Typhoon Talas that struck central and western Japan [*Yamada et al.*, 2012] on 3 and 4 September 2011. The landslide volume was estimated to be 8.2×10^6 m^3 [*Yamada et al.*, 2012] corresponding to a mass of 2.1×10^{10} kg [*Yamada et al.*, 2013]. Observations of the deposit and force history inversion [*Yamada et al.*, 2013; *Ekström and Stark*, 2013] show a simple sliding geometry, with a mass that slid straight toward the northwest and stopped when it hit the opposite valley wall. The moment when the sliding mass hit the opposite valley wall is marked by an amplitude peak in the short-period seismic signal [*Yamada et al.*, 2013].

Bingham Canyon Mine. A sequence of two landslides occurred in the Bingham Canyon Mine, located close to Salt Lake City (Utah, USA), on 10 April 2013 [*Pankow et al.*, 2014; *Hibert et al.*, 2014b]. The first failure occurred at 03:31 UT and the subsequent one at 05:06 UT. The masses of the first and the second landslides, inferred from inversion of the long-period seismic waves, are 7×10^{10} kg and 4.5×10^{10} kg, respectively. Both landslides where stopped by the mine wall and the collision generated clearly identifiable amplitude peaks in the short-period seismic signals [*Hibert et al.*, 2014b]. Detailed analyses of the broadband seismic signals generated by both events can be found in *Pankow et al.* [2014] and *Hibert et al.* [2014b].

Hsiǎolín. The Hsiǎolín landslide occurred on 8 August 2009 at 22:16 UT during the period when Typhoon Morakot hit Taiwan and caused 474 fatalities in the Hsiǎolín village [*Lin et al.*, 2010; *Kuo et al.*, 2011; *Lo et al.*, 2011]. The bulk of the landslide moved straight to the valley and formed a dam on the Cishan River [*Kuo et al.*, 2011; *Lo et al.*, 2011]. A small part of the moving mass may have taken a secondary path located south from the main one. The volume of the main body of the landslide is estimated to be $24 \pm 2 \times 10^6$ m^3 [*Kuo et al.*, 2011], corresponding to a mass of 6×10^{10} kg [*Ekström and Stark*, 2013].

Fāngtúnshān. The Fāngtúnshān event was also part of the sequence of landslides caused by Typhoon Morakot in Taiwan. It occurred on 9 August 2009 at 09:31 UT. The mobilized mass is estimated at 1.3×10^{11} kg [*Ekström and Stark*, 2013].

Hubbard. The Hubbard landslide (Alaska-Yukon, USA-Canada Border) occurred on 21 May 2012 at 14:25 UT. The scaling law established by *Ekström and Stark* [2013] between the maximum of the inverted force exerted by the landslide on the slope and its mass gives a rough estimate of the latter at 8×10^{10} kg.

Mount Dall. The Mount Dall (Alaska, USA) landslide occurred on 9 April 1999 at 15:15 UT. This event was seismically retrieved by a detection and location algorithm applied to global data recorded from 1999 to 2001.

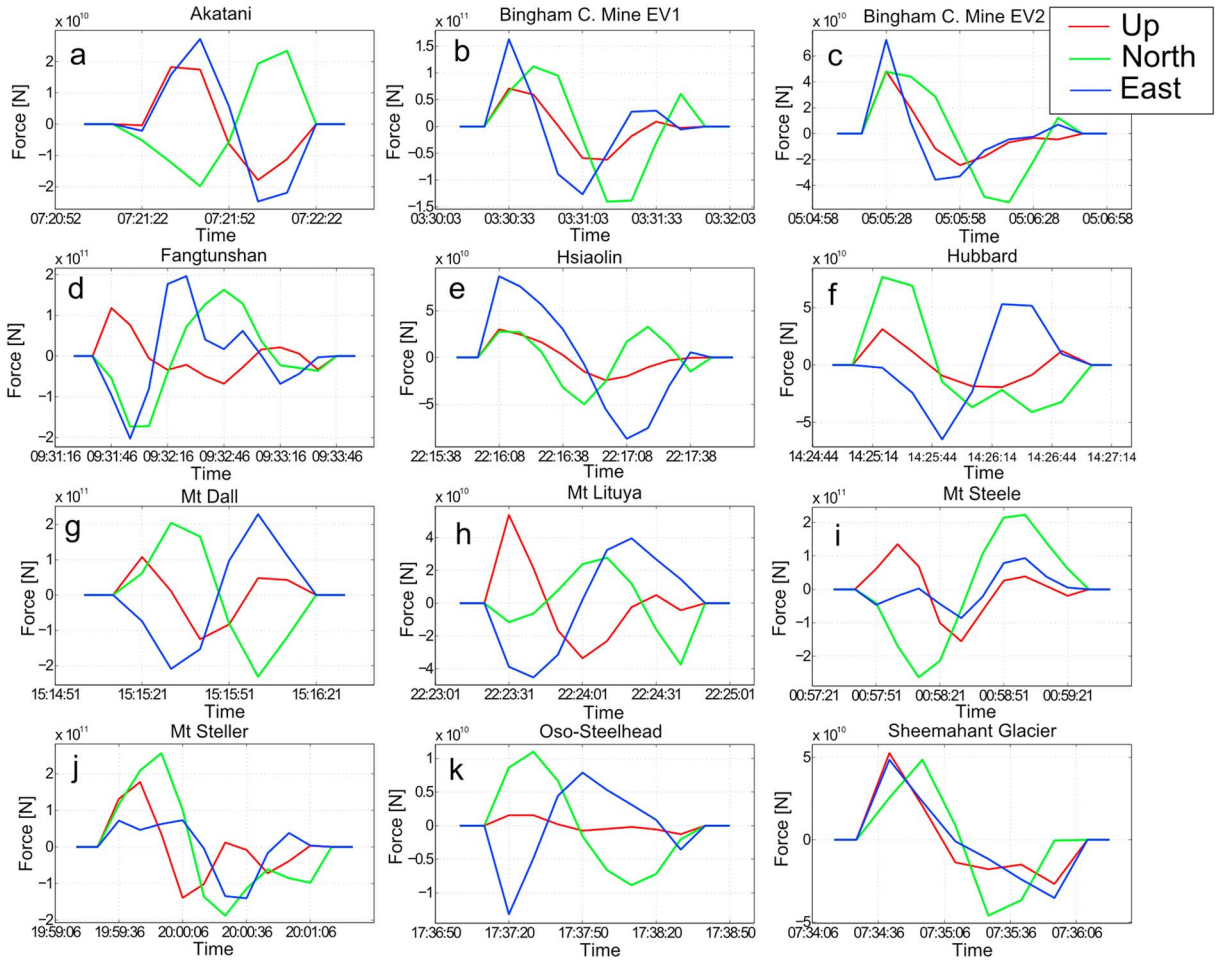

Figure A1. Inverted landslide force history (LFH) for the (a) Akatani, (b) first Bingham Canyon Mine, (c) second Bingham Canyon Mine, (d) Fāngtúnshān, (e) Hsiǎolín, (f) Hubbard, (g) Mount Dall, (h) Mount Lituya, (i) Mount Steele, (j) Mount Steller, (k) Oso-Steelhead, and (l) Sheemahant landslides.

Mount Lituya. The Mount Lituya (Glacier Bay, Alaska, USA) landslide was seismically detected but first misidentified as a tectonic earthquake. This large rockslope failure occurred on 11 June 2012 at 22:23 UT and is characterized by a very long runout of more than 9 km over the Hopkins Glacier. The landslide mass is estimated to be approximately 2×10^10 kg [*Ekström and Stark*, 2013].

Mount Steele. The north face of Mount Steele (Saint Elias Mountains, Yukon, Canada) collapsed on 27 July 2007 at 00:57 UT, forming a rock-ice avalanche that traveled almost 6 km in a nearly straight line, crossed the Steele Glacier, and stopped [*Lipovsky et al.*, 2008]. The mobilized volume is estimated between 27×10^6 m^3 and 80×10^6 m^3 [*Lipovsky et al.*, 2008; *Huggel et al.*, 2012] and the mass at 1.08×10^{11} kg [*Ekström and Stark*, 2013].

Mount Steller. A part of the summit of the Mount Steller (Chugach Mountains, Alaska, USA) collapsed on 14 September 2005 at 19:59 UT. The volume mobilized is estimated between 40×10^6 m^3 and 60×10^6 m^3 [*Huggel et al.*, 2008a, 2008b] and the mass at 8.1×10^{10} kg [*Ekström and Stark*, 2013]. The bulk of the rock-ice avalanche traveled 10 km with no significant changes of direction before coming to rest [*Huggel et al.*, 2008a, 2008b; *Moretti et al.*, 2012].

Oso-Steelhead. The Oso-Steelhead landslide, located near Seattle (Washington, USA), occurred on 22 March 2014 at 17:37 UT, after a period of heavy rainfall, and destroyed the "Steelhead Haven" community resulting in 44 fatalities [*Keaton et al.*, 2014; *Iverson et al.*, 2015]. The main failure has a simple geometry, with mass starting to slide toward the southeast, slightly turning to the south during the movement which ended in the valley bottom, blocking the stream of the Stillaguamish River and forming a dam. Ground observations and inference from long-period surface waves inversion give an estimate of the volume between 7×10^6 m^3 and

10×10^6 m^3 and a corresponding mass between 1.4×10^{10} kg and 2.6×10^{10} kg [*Keaton et al.*, 2014; *Hibert et al.*, 2015; *Iverson et al.*, 2015].

Sheemahant Glacier. The Sheemahant Glacier landslide occurred on 9 July 2010 at 7:35 UT in British Columbia, Canada. This landslide was first seismically detected and then identified on satellite images. Inversion of the long-period seismic waves provided an estimate of the mass of this landslide at 8.1×10^{10} kg [*Ekström and Stark*, 2013]. Its runout distance is approximately 3 km, and the slide did not undergo significant flow direction changes along its trajectory.

Acknowledgments

This work was supported by the US National Science Foundation Division of Earth Sciences and the Geomorphology and Land-use Dynamics/Geophysics programs under awards 1227083 and 1148176 and the U.S. National Science Foundation Division of Civil, Mechanical, and Manufacturing Innovation and the Hazards SEES program under award 1331499. We thank the operators of the seismic UU, PW, Hi-net, F-net, and AK networks for collecting the data used in this study and the IRIS Data Management System for providing easy access to the data. Data are available through the IRIS portal (http://ds.iris.edu/SeismiQuery/) and the Hi-Net portal following registration (http://www.hinet.bosai.go.jp/). The authors gratefully acknowledge Jackie Caplan-Auerbach, Maxime Farin, and an anonymous reviewer for insightful reviews. We also would like to thank the Editors for their substantial comments, which helped to improve this manuscript.

References

Aki, K., and B. Chouet (1975), Origin of coda waves: Source, attenuation, and scattering effects, *J. Geophy. Res.*, *80*(23), 3322–3342.

Aki, K., and P. G. Richards (1980), *Quantitative Seismology*, vol. 1, WH Freeman and Co., San Francisco, Calif.

Allstadt, K. (2013), Extracting source characteristics and dynamics of the August 2010 Mount Meager landslide from broadband seismograms, *J. Geophy. Res. Earth Surf.*, *118*, 1472–1490, doi:10.1002/jgrf.20110.

Brodsky, E. E., E. Gordeev, and H. Kanamori (2003), Landslide basal friction as measured by seismic waves, *Geophys. Res. Lett.*, *30*(24), 2236, doi:10.1029/2003GL018485.

Burtin, A., N. Hovius, D. T. Milodowski, Y.-G. Chen, Y.-M. Wu, C.-W. Lin, H. Chen, R. Emberson, and P.-L. Leu (2013), Continuous catchment-scale monitoring of geomorphic processes with a 2-D seismological array, *J. Geophys. Res. Earth Surf.*, *118*, 1956–1974, doi:10.1002/jgrf.20137.

Calder, E., R. Luckett, R. Sparks, and B. Voight (2002), Mechanisms of lava dome instability and generation of rockfalls and pyroclastic flows at Soufriere Hills Volcano, Montserrat, *Geol. Soc. London Mem.*, *21*(1), 173–190.

Chen, C.-H., W.-A. Chao, Y.-M. Wu, L. Zhao, Y.-G. Chen, W.-Y. Ho, T.-L. Lin, K.-H. Kuo, and J.-M. Chang (2013), A seismological study of landquakes using a real-time broad-band seismic network, *Geophys. J. Intern.*, *194*(2), 885–898.

Clouard, V., J.-E. Athanase, and C. Aubaud (2013), Physical characteristics and triggering mechanisms of the 2009–2010 landslide crisis at Montagne Pelée volcano, Martinique: Implication for erosional processes and debris-flow hazards, *Bulletin de la Société Géologique de France*, *184*(1–2), 155–164.

Coe, J. A., R. L. Baum, K. E. Allstadt, B. F. Kochevar, R. G. Schmitt, M. L. Morgan, J. L. White, B. T. Stratton, T. A. Hayashi, and J. W. Kean (2016), Rock-avalanche dynamics revealed by large-scale field mapping and seismic signals at a highly mobile avalanche in the West Salt Creek valley, western Colorado, *Geosphere*, *12*(2), 607–631.

Dammeier, F., J. R. Moore, F. Haslinger, and S. Loew (2011), Characterization of alpine rockslides using statistical analysis of seismic signals, *J. Geophy. Res.*, *116*, F04024, doi:10.1029/2011JF002037.

Dammeier, F., J. R. Moore, C. Hammer, F. Haslinger, and S. Loew (2016), Automatic detection of alpine rockslides in continuous seismic data using Hidden Markov Models, *J. Geophys. Res. Earth Surf.*, *121*, 351–371, doi:10.1002/2015JF003647.

Deparis, J., D. Jongmans, F. Cotton, L. Baillet, F. Thouvenot, and D. Hantz (2008), Analysis of rock-fall and rock-fall avalanche seismograms in the French Alps, *Bull. Seismol. Soc. Am.*, *98*(4), 1781–1796, doi:10.1785/0120070082.

Ekström, G., and C. P. Stark (2013), Simple scaling of catastrophic landslide dynamics, *Science*, *339*, 1416–1419, doi:10.1126/science.1232887.

Favreau, P., A. Mangeney, A. Lucas, G. Crosta, and F. Bouchut (2010), Numerical modeling of landquakes, *Geophys. Res. Lett.*, *37*, L15305, doi:10.1029/2010GL043512.

Fukao, Y. (1995), Single-force representation of earthquakes due to landslides or the collapse of caverns, *Geophys. J. Intern.*, *122*, 243–248, doi:10.1111/j.1365-246X.1995.tb03551.x.

Helmstetter, A., and S. Garambois (2010), Seismic monitoring of Séchilienne rockslide (French Alps): Analysis of seismic signals and their correlation with rainfalls, *J. Geophy. Res.*, *115*, F03016, doi:10.1029/2009JF001532.

Hibert, C., A. Mangeney, G. Grandjean, and N. M. Shapiro (2011), Slope instabilities in Dolomieu crater, Réunion Island: From seismic signals to rockfall characteristics, *J. Geophy. Res.*, *116*, F04032, doi:10.1029/2011JF002038.

Hibert, C., et al. (2014a), Automated identification, location, and volume estimation of rockfalls at Piton de la Fournaise volcano, *J. Geophys. Res. Earth Surf.*, *119*, 1082–1105, doi:10.1002/2013JF002970.

Hibert, C., G. Ekström, and C. P. Stark (2014b), Dynamics of the Bingham Canyon Mine landslides from seismic signal analysis, *Geophys. Res. Lett.*, *41*, 4535–4541, doi:10.1002/2014GL060592.

Hibert, C., C. Stark, and G. Ekström (2015), Dynamics of the Oso-Steelhead landslide from broadband seismic analysis, *Nat. Hazards and Earth Syst. Sci.*, *15*(6), 1265–1273.

Huggel, C., S. Gruber, S. Caplan-Auerbach, R. L. Wessels, and B. F. Molnia (2008a), The 2005 Mt. Steller, Alaska, rock-ice avalanche: A large slope failure in cold permafrost, in *9th International Conference on Permafrost, Fairbanks*., pp. 747–752, Alaska, 29 June.

Huggel, C., S. Caplan-Auerbach, and R. L. Wessels (2008b), Recent extreme avalanches: Triggered by climate change?, *EOS, Trans. AGU*, *89*(47), 469–470.

Huggel, C., J. J. Clague, and O. Korup (2012), Is climate change responsible for changing landslide activity in high mountains?, *Earth Surf. Processes Landforms*, *37*, 77–91.

Iverson, R., et al. (2015), Landslide mobility and hazards: Implications of the 2014 Oso disaster, *Earth and Planetary Sci. Lett.*, *412*, 197–208.

Kanamori, H., and J. W. Given (1982), Analysis of long-period seismic waves excited by the May 18, 1980, eruption of Mount St. Helens—A terrestrial monopole?, *J. Geophy. Res.*, *87*(B7), 5422–5432, doi:10.1029/JB087iB07p05422.

Kanamori, H., J. W. Given, and T. Lay (1984), Analysis of seismic body waves excited by the Mount St. Helens eruption of May 18, 1980, *J. Geophy. Res.*, *89*(B23), 1856–1866.

Keaton, J. R., J. Wartman, S. Anderson, J. Benoît, J. deLaChapelle, R. Gilbert, and D. R. Montgomery (2014), The 22 March 2014 Oso Landslide, Snohomish County, Washington, GEER report, NSF Geotechnical Extreme Events Reconnaissance, 172 pp.

Kuo, C.-Y., Y.-C. Tai, C.-C. Chen, K.-J. Chang, A.-Y. Siau, J.-J. Dong, R.-H. Han, T. Shimamoto, and C.-T. Lee (2011), The landslide stage of the Hsiaolin catastrophe: Simulation and validation, *J. Geophy. Res.*, *116*, F04007, doi:10.1029/2010JF001921.

Levy, C., A. Mangeney, F. Bonilla, C. Hibert, E. S. Calder, and P. J. Smith (2015), Friction weakening in granular flows deduced from seismic records at the Soufrière Hills Volcano, Montserrat, *J. Geophy. Res. Solid Earth*, *120*, 7536–7557, doi:10.1002/2015JB012151.

Lin, C.-H., H. Kumagai, M. Ando, and T.-C. Shin (2010), Detection of landslides and submarines slumps using broadband seismic networks, *Geophys. Res. Lett.*, *37*, L22309, doi:10.1029/2010GL044685.

Lipovsky, P. S., et al. (2008), The July 2007 rock and ice avalanches at Mount Steele, St. Elias Mountains, Yukon, Canada, *Landslides*, *5*, 445–455, doi:10.1007/s10346-008-0133-4.

Lo, C.-M., M.-L. Lin, C.-L. Tang, and J.-C. Hu (2011), A kinematic model of the Hsiaolin landslide calibrated to the morphology of the landslide deposit, *Eng. Geol.*, *123*(1), 22–39.

Luckett, R., B. Baptie, and J. Neuberg (2002), The relationship between degassing and rockfall signals at Soufriere Hills Volcano, Montserrat, *Geol. Soc. London Mem.*, *21*(1), 595–602.

McSaveney, M. J. (2002), Recent rockfalls and rock avalanches in Mount Cook National Park, New Zealand, *Rev. Eng. Geol.*, *15*, 35–70.

Moretti, L., A. Mangeney, Y. Capdeville, E. Stutzmann, C. Huggel, D. Schneider, and F. Bouchut (2012), Numerical modeling of the Mount Steller landslide flow history and of the generated long period seismic waves, *Geophys. Res. Lett.*, *39*, L16402, doi:10.1029/2012GL052511.

Norris, R. D. (1994), Seismicity of rockfalls and avalanches at three Cascade Range volcanoes: Implications for seismic detection of hazardous mass movements, *Bull. Seismol. Soc. Am.*, *84*(6), 1925–1939.

Pankow, K. L., J. R. Moore, J. M. Hale, K. D. Koper, T. Kubacki, K. M. Whidden, and M. K. McCarter (2014), Massive landslide at Utah copper mine generates wealth of geophysical data, *GSA Today*, *24*(1), 4–9, doi:10.1130/GSATG191A.1.

Ratdomopurbo, A., and G. Poupinet (2000), An overview of the seismicity of Merapi volcano (Java, Indonesia), 1983–1994, *J. Volcanol. Geotherm. Res.*, *100*(1), 193–214.

Richter, C. F. (1935), An instrumental earthquake magnitude scale, *Bull. Seismol. Soc. Am.*, *25*(1), 1–32.

Richter, C. F. (1958), *Elementary Seismology*, WH Freeman and Co., San Francisco, Calif.

Schneider, D., P. Bartelt, J. Caplan-Auerbach, M. Christen, C. Huggel, and B. W. McArdell (2010), Insights into rock-ice avalanche dynamics by combined analysis of seismic recordings and a numerical avalanche model, *J. of Geophy. Res.*, *115*, F04026, doi:10.1029/2010JF001734.

Suriñach, E., I. Vilajosana, G. Khazaradze, B. Biescas, G. Furdada, and J. M. Vilaplana (2005), Seismic detection and characterization of landslides and other mass movements, *Nat. Haz. and Earth Syst. Sci.*, *5*, 791–798, doi:10.5194/nhess-5-791-2005.

Tripolitsiotis, A., A. Daskalakis, S. Mertikas, D. Hristopulos, Z. Agioutantis, and P. Partsinevelos (2015), Detection of small-scale rockfall incidents using their seismic signature, in *Third International Conference on Remote Sensing and Geoinformation of the Environment*, pp. 953,519–953,519, Int. Soc. for Optics and Photonics, Bellingham, Wash.

Vilajosana, I., E. Suriñach, A. Abellán, G. Khazaradze, D. Garcia, and J. Llosa (2008), Rockfall induced seismic signals: Case study in Montserrat, Catalonia, *Nat. Haz. and Earth Syst. Sci.*, *8*, 805–812, doi:10.5194/nhess-8-805-2008.

Yamada, M., Y. Matsushi, M. Chigira, and J. Mori (2012), Seismic recordings of landslides caused by Typhoon Talas (2011), Japan, *Geophys. Res. Lett.*, *39*, L13301, doi:10.1029/2012GL052174.

Yamada, M., H. Kumagai, Y. Matsushi, and T. Matsuzawa (2013), Dynamic landslide processes revealed by broadband seismic records, *Geophys. Res. Lett.*, *40*, 2998–3002, doi:10.1002/grl.50437.

Zhao, J., et al. (2012), Model space exploration for determining landslide source history from long-period seismic data, *Pure and Applied Geophysics*, 1–25.

Zimmer, V. L., and N. Sitar (2015), Detection and location of rock falls using seismic and infrasound sensors, *Eng. Geol.*, *193*, 49–60.